ADVANCED ENERGY MATERIALS
www.advenergymat.de

Tungsten–Carbon Nanotube Composite Photonic Crystals as Thermally Stable Spectral-Selective Absorbers and Emitters for Thermophotovoltaics

Kehang Cui, Paul Lemaire, Hangbo Zhao, Timothy Savas, Gregory Parsons, and A. John Hart**

Thermophotovoltaics (TPVs) is a promising energy conversion technology which can harvest wide-spectrum thermal radiation. However, the manufacturing complexity and thermal instability of the nanophotonic absorber and emitter, which are key components of TPV devices, significantly limit their scalability and practical deployment. Here, tungsten–carbon nanotube (W-CNT) composite photonic crystals (PhCs) exhibiting outstanding spectral and angular selectivity of photon absorbance and thermal emission are presented. The W-CNT PhCs are fabricated by nanoscale holographic interferometry-based patterning of a thin-film catalyst, modulated chemical vapor deposition synthesis of high-density CNT forest nanostructures, and infiltration of the CNT forests with tungsten via atomic layer deposition. Owing to their highly stable structure and composition, the W-CNT PhCs exhibit negligible degradation of optical properties after annealing for 168 hours at 1273 K, which exceeds all previously reported high-temperature PhCs. Using the measured spectral properties of the W-CNT PhCs, the system efficiency of a GaSb-based solar TPV (STPV) that surpasses the Shockley–Queisser efficiency limit at modest operating temperatures and input powers is numerically predicted. These findings encourage further practical development of STPVs, and this scalable fabrication method for composite nanostructures could find other applications in electromagnetic metamaterials.

Materials with controlled photon absorption and thermal emission have wide application in the fields of energy-efficient lighting,[1–3] molecular sensing,[4–7] radiative cooling,[8–10] and energy harvesting.[11–15] Thermophotovoltaic (TPV) systems[16] rely on PhC surfaces to convert broad-band solar irradiation or combustion heat to narrow-band near infrared thermal emission which matches the electronic bandgaps of photovoltaic (PV) cells. By harvesting sub-bandgap photons and hot carriers, TPVs can exceed the Shockley–Queisser (SQ) efficiency limit[17] and have output energy density as high as 10^5 W m^{-2}.[18]

Use of engineered nanophotonic surfaces as absorbers and emitters has significantly improved the power conversion efficiencies of TPV devices from below 1% to 6.7%.[12,13,18,19] However, the experimentally demonstrated efficiencies of TPV systems are still far below their theoretical capability, in large part due to parasitic thermal losses.[12,13,19] Absorbers and emitters for TPVs are usually manufactured by deep reactive ion etching or scanning electron beam lithography, requiring clean room facilities and expensive equipment which limits the practical device area.[20] Recent studies have demonstrated absorbers and emitters fabricated by nanoimprint lithography,[21] nanopyramid template stripping,[22] nanoparticle dewetting,[23] and self-assembled reverse opal methods.[24] All of these techniques are intrinsically more scalable than lithography-based patterning, but cannot replicate the precision of the latter, thereby sacrificing optical selectivity.

Maintaining the submicron characteristic dimensions of PhCs at high operating temperatures (>800 °C) over a long duration is another technological difficulty. For 1D superlattice PhCs, a slight mismatch in the thermal expansion coefficient between layers can cause delamination due to thermomechanical stress.[25–27] Refractory metals typically used in 2D and 3D PhCs (e.g., tungsten, ruthenium, and tantalum) suffer from surface diffusion and structural degradation at high operating temperatures,[28] causing losses of selectivity

Dr. K. Cui, Dr. H. Zhao, Prof. A. J. Hart
Department of Mechanical Engineering and Laboratory for Manufacturing and Productivity
Massachusetts Institute of Technology
Cambridge, MA 02139, USA
E-mail: cuik@mit.edu; ajhart@mit.edu
Dr. P. Lemaire, Prof. G. Parsons
Department of Chemical and Biomolecular Engineering
North Carolina State University
Raleigh, NC 27606, USA
Dr. T. Savas
Research Laboratory of Electronics
Massachusetts Institute of Technology
Cambridge, MA 02139, USA
The ORCID identification number(s) for the author(s) of this article can be found under https://doi.org/10.1002/aenm.201801471.

DOI: 10.1002/aenm.201801471

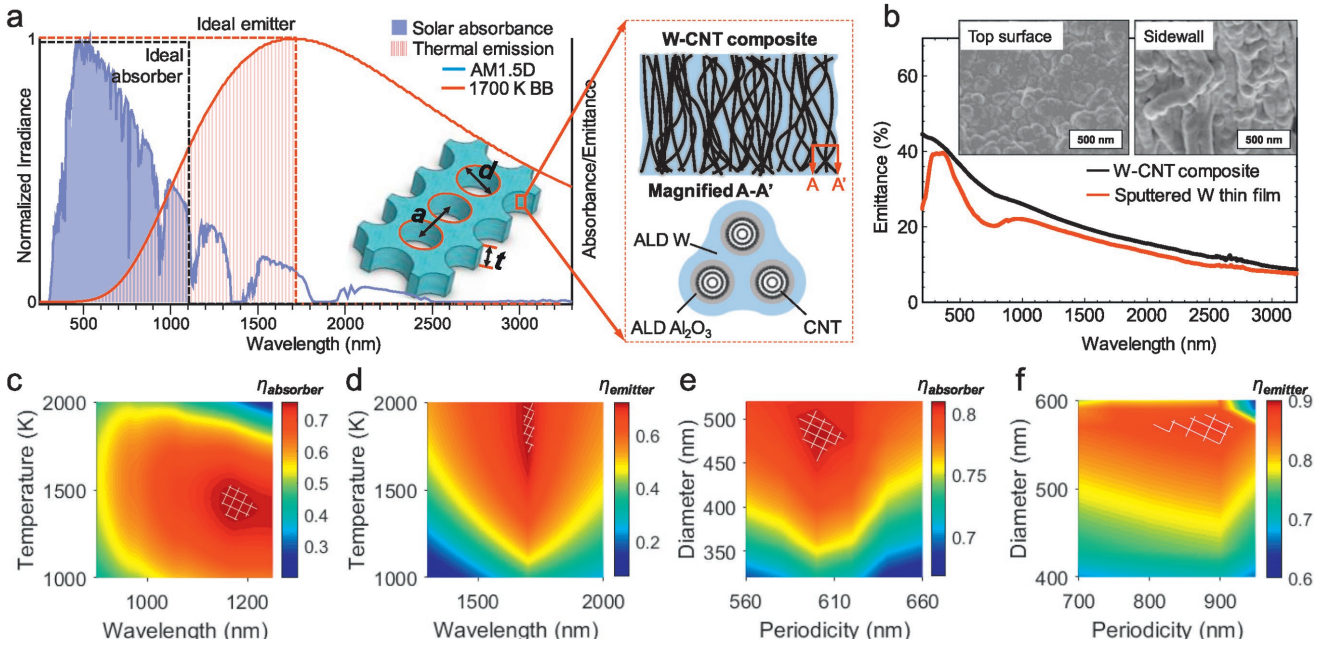

Figure 1. Design of W-CNT PhCs. a) Spectral selectivity of ideal absorber and emitter for STPV system. Inset: schematic of geometric parameters (periodicity a, nanocavity diameter d, and thickness t) of the W-CNT PhCs that determine the spectral selectivity, and schematic of the W-CNT composite material. b) UV–vis–NIR reflection spectra of the top surface of the unpatterned W-CNT composite and the W thin film sputter-deposited on a polished Si/SiO_2 substrate. Inset: SEM images of the top surface and the sidewall of the unpatterned W-CNT composite. c,d) Numerical optimization of the spectral cutoffs of the absorber and emitter. e,f) Numerical optimization of the periodicity a and nanocavity diameter d for the design of the W-CNT nanophotonic absorber and emitter.

in photon absorption and thermal emission. Coatings such as HfO_2[24,29–32] can enhance thermal stability, yet elemental scarcity and high cost potentially prevent their use at scale.[33,34]

Here we propose a scalable approach for the fabrication of PhCs for use in TPV systems, via formation of tungsten–carbon nanotube (W-CNT) composite surfaces having high spectral selectivity and exceptional thermal stability. The W-CNT PhCs are designed to function as the selective absorber and emitter in a standard solar thermophotovoltaic (STPV) system using an external GaSb PV cell (bandgap 0.7 eV). As shown in **Figure 1**a, both the absorber and emitter have spectral cutoffs, together serving as a thermal rectifier. In a STPV system, the absorber ideally converts full-spectrum solar irradiation to thermal energy with unity absorbance, and serves as a thermal insulation layer for the emitter to guarantee unidirectional thermal emission to the PV cell below. An ideal emitter then quenches the radiation below the bandgap of the PV cell (zero emittance) and enhances the thermal emission elsewhere (unity emittance). The spectral selectivity of the absorber and emitter can be tailored via the nanocavity diameter d, periodicity a and thickness t (Figure 1a).

Our approach is to use nanopatterned vertically aligned carbon nanotubes (VACNTs) as a nanoporous scaffold for infiltration of a refractory metal (W), forming thermally stable composite PhCs. Uniform, high-density CNT growth is critical to achieve submicron VACNT features and form precise PhC scaffolds. A dynamic chemical vapor deposition (CVD) process with carbon pre-conditioning of the catalyst (see the Experimental Section) was used to grow VACNTs with much higher density and alignment (HD-VACNTs) than the conventional CVD process, as compared in Figure S1 of the Supporting Information. The surface of the reference low-density VACNTs is a blackbody absorbing light omnidirectionally, similar to previous studies,[35,36] while the surface of the HD-VACNTs is shiny and reflective (Figure S1c,d, Supporting Information). UV–vis–NIR reflection spectra (Figure S1e, Supporting Information) demonstrate that the reflectivity of the top surface of the HD-VACNTs (≈0.2) is ≈100-fold greater than that of the reference VACNTs, and is similar to that of graphite[37] and glassy carbon.[38–41]

After HD-VACNT growth, the W-CNT composite material is formed by atomic layer deposition (ALD) of ≈2 nm thick Al_2O_3 and ≈20 nm thick W onto the CNTs. The SEM images in the insets of Figure 1b demonstrate that the top surface of the W-CNT composite is smooth and solid, while the sidewall is composed of Al_2O_3-coated CNTs embedded in the W matrix. To examine the validity of the W-CNT composite material for the fabrication of 2D PhCs, UV–vis–NIR spectra of a sputtered W thin film and the top surface of the unpatterned W-CNT composite are compared (Figure 1b), and match well with each other in the visible and NIR ranges. The top surface of the unpatterned W-CNT composite has even greater absorptivity below 400 nm, which may be attributed to roughness-induced Mie scattering.

Design of the W-CNT nanophotonic absorber and emitter for the STPV system has two main steps: 1) optimization of the spectral cutoff position, and 2) optimization of the geometric parameters (d, a, and t) of the W-CNT PhCs to maximize the absorber and emitter figures of merit. The absorber figure of merit ($\eta_{absorber}$) is defined as the ratio of the stored thermal

energy to the total solar irradiance multiplied by the Carnot efficiency

$$\eta_{\text{absorber}} = \left(1-\frac{T}{T_a}\right)\left[C\int_{\text{solar}} d\lambda\alpha(\lambda)I_s(\lambda) - \int_{\text{BB}} d\lambda\alpha(\lambda)I_{\text{BB}}(\lambda,T)\right]/\left[C\int_{\text{solar}} d\lambda I_s(\lambda)\right] \quad (1)$$

where C is the number of suns, λ is the wavelength, I_s is the solar irradiance, I_{BB} is the blackbody radiation, T_a is the ambient temperature (300 K), and α is the spectral absorbance of the absorber. The emitter figure of merit (η_{emitter}) is the ratio of the energy contained in the electron-hole pairs in the PV cell to the total thermal energy irradiated from the emitter, given by

$$\eta_{\text{emitter}} = \int_{E_g}^{\infty}\frac{E_g}{E}dE\varepsilon(E)I_{\text{BB}}(E,T)\Big/\int_0^{\infty}dE\varepsilon(E)I_{\text{BB}}(E,T) \quad (2)$$

where ε is the spectral emittance of the emitter, E is photon energy, and E_g is the bandgap of the GaSb cell, i.e., 0.7 eV. The spectral cutoff positions are optimized using step function-like absorbance and emittance

$$\alpha_p,\varepsilon_p(\lambda) = \begin{cases} 0.95; & \lambda \le \lambda_{\text{cutoff}} \\ 0.05; & \lambda > \lambda_{\text{cutoff}} \end{cases} \quad (3)$$

where α_p and ε_p respectively denote the absorbance and emittance, and λ_{cutoff} is the cutoff wavelength. The values 0.95 and 0.05 adopted here are based on the highest α_p, $\varepsilon_p(\lambda \le \lambda_{\text{cutoff}})$ and lowest α_p, $\varepsilon_p(\lambda > \lambda_{\text{cutoff}})$ among previous studies.[15,19,20,22,24,26,29,32,42,43]

The calculated values of η_{absorber} versus the spectral cutoff and STPV working temperature (under 100 suns illumination) are shown in Figure 1c. The maximum η_{absorber} of 75.6% is predicted at a cutoff position of 1171 nm and operating temperature of 1400 K. The optimal cutoff position is dictated by the tradeoff between solar absorption and thermal emission at operating temperature. For the emitter, a spectral cutoff position of 1673 nm (Figure 1d) is chosen to match the electronic bandgap of GaSb PV cells (0.7 eV). At this cutoff position, η_{emitter} reaches the maximum value for each operating temperature from 1000 to 2000 K.

Next, the W-CNT PhCs were designed to realize the desired spectral cutoffs calculated above, using a finite-difference time domain method (FDTD, incorporated via the MIT Electromagnetic Equation Propagation (MEEP) package.[44] The material dispersion was extracted from the data in Figure 1b using the Lorentz–Drude model (see the Experimental Section). The effect of the thickness t on the spectral selectivity of two representative PhC designs (a = 1.3, d = 1.1 μm; and a = 1.1, d = 0.9 μm, chosen from ref. [15]) is shown in Figure S2 of the Supporting Information. When the thickness increases from 2 to 12 μm, the absorbance/emittance at the wavelengths below the spectral cutoff is enhanced significantly. This is because the increased PhC thickness reduces photon transmission and increases photon-nanocavity interaction time to realize cavity resonator modes.[43,45] However, further increasing the thickness to 15 and 20 μm does not appreciably change the absorbance or emittance for both PhC designs. With the thickness t set as 15 μm, the diameter and periodicity of the nanocavity are subsequently optimized. The d/a of the nanocavities in the W-CNT nanophotonic absorber and emitter are chosen to be 480/600 nm and 640/900 nm, respectively, giving η_{absorber} and η_{emitter} both greater than 80%, as shown in Figure 1e,f.

To realize the W-CNT PhCs according to our computational design, nanopatterned CNTs are grown from supported catalyst films (Fe/Al_2O_3) patterned by holographic interferometry (see the Experimental Section), followed by ALD coating with Al_2O_3 and W, resulting in uniform, high aspect ratio composite PhCs with precise nanocavity dimensions. The process is schematically depicted in **Figure 2**a. For CNT synthesis, the substrate with the nanopatterned catalyst film is rapidly inserted to the CVD reactor using an automated mechanism after the furnace reaches the target temperature and stable atmosphere ($C_2H_4/He/H_2O/H_2$); under these conditions, the CNTs grow rapidly (≈2 μm s^{-1}), and the final CNT thickness of 15 μm is controlled by withdrawing the substrate from the reactor at a set time. Next, Al_2O_3 and W coatings are sequentially deposited by ALD. For Al_2O_3, use of ozone as the oxidizing agent[46,47] causes uniform adsorption of the organometallic precursor (trimethylaluminum, TMA), resulting in a thin, conformal Al_2O_3 coating which subsequently serves as a seed layer for W deposition. The result is a uniform composite PhC with the nanopatterned VACNTs embedded in a nanocrystalline W matrix.

As shown in Figure 2b,c, the diameter and periodicity of the nanocavities in the as-grown nanopatterned VACNTs for the W-CNT nanophotonic absorber and emitter are highly uniform, measuring 524 ± 12 and 602 ± 13 nm as well as 675 ± 11 and 894 ± 14 nm, respectively. The VACNT wall thickness between adjacent cylindrical nanocavities is only 78 ± 10 nm, which to our knowledge is the smallest freestanding CNT forest structure reported in literature to date.[48–50] At the thickness of 15 μm, the walls between nanocavities reach an aspect ratio (AR) of ≈200, in only 10 s of CVD synthesis after insertion of the substrate to the heated reactor. High-aspect ratio metal-based PhCs fabricated by top-down processes are challenged by inevitable sidewall undercutting in anisotropic etching,[51,52] which in literature are limited to 8 μm.[53–56] SEM images show that the nanocavity diameters of the W-CNT absorber (479 ± 17 nm) and emitter (633 ± 19 nm) are uniform through the thickness.

As shown by the UV–vis–NIR spectra in **Figure 3**a, the W-CNT nanophotonic absorber has a sharp spectral cutoff at 1130 nm (1.1 eV), and near-unity absorbance is observed above 1.2 eV. The W-CNT nanophotonic emitter exhibits a steep spectral cutoff at 1600 nm and near-unity emittance below 1300 nm (Figure 3b). The measured cutoff frequencies generally match the corresponding FDTD numerical simulations, but the experimental values of the absorbance and emittance are slightly higher than the simulation results over the whole spectral range, likely owing to diffuse reflection from the top surface.[26] Greater absorbance and emittance in the longer wavelength range cause more re-emission to the environment and sub-bandgap photon emission to the PV cell, which would decrease the STPV system efficiency. This could be mitigated by surface polishing[57–59] or further modification of the CVD process.

The efficiency of an STPV system is also influenced by the incident angle of the thermal emission upon the PV cell.

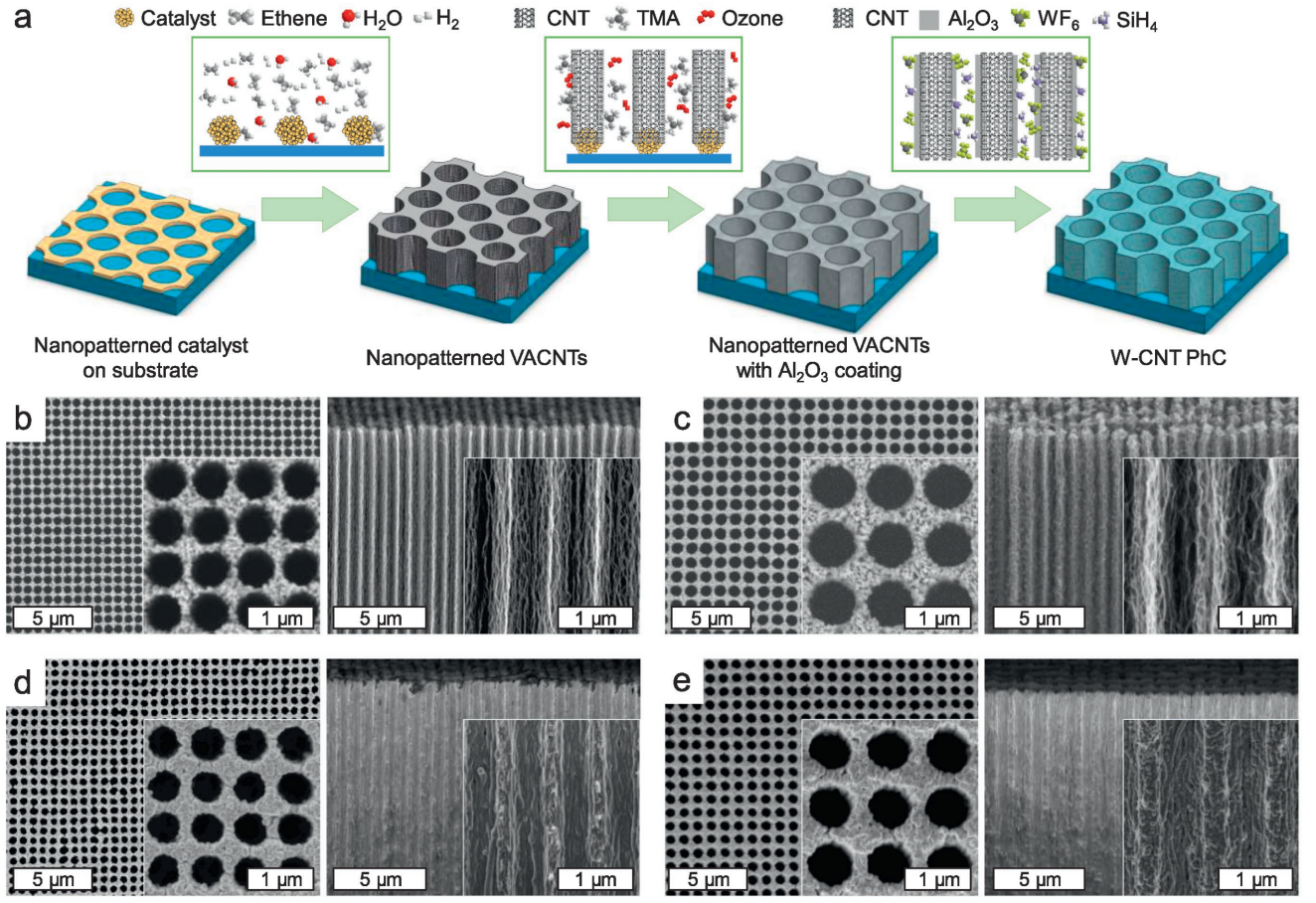

Figure 2. Fabrication of W-CNT PhCs. a) Schematic key steps of fabrication process (note the CNTs are shown as parallel and equally spaced to simplify the depiction at the nanoscale). b,c) Top-view and side-view SEM images of the as-grown nanopatterned VACNT arrays for the W-CNT absorber and emitter. d,e) Top-view and side-view SEM images of the W-CNT absorber and emitter after ALD coating.

When the thermal emission impinges on the PV cell at oblique angles, the surface recombination rate of the electron-hole pairs increases,[60–62] resulting in considerable losses in the system efficiency and power output density. The angular-dependent absorbance and emittance are measured by UV–vis–NIR spectroscopy, as shown in Figure 3c,d. The average absorbance and emittance (from 300 to 800 nm) both exceed 0.8 in the angle range of 0° to 22.5° and decline drastically when the incident angle further increases, which is consistent with the FDTD simulations (Figure S5, Supporting Information). Therefore, we conclude that the W-CNT absorber can provide a 45° acceptance cone for the concentrator design and limit the radiation loss to the environment outside the acceptance cone. Further, the W-CNT emitter can effectively mitigate nonradiative recombination (Shockley–Read–Hall recombination) in the PV cell,[60–62] which benefits the power output density of the STPV system.

The optical and structural stability of PhCs at high temperatures is critical to the practical application of STPV systems.[29,31,56,63] In Figure 3a,b, we also illustrate that, after annealing at 1273 K for up to 168 h (10^{-3} Torr vacuum with He protection), the spectral selectivity does not deteriorate for both the W-CNT nanophotonic absorber and emitter. Our measurements show no change in the absorber efficiency ($\eta_{absorber}$ = 84%) after 168 h annealing at 1273 K. The emitter efficiency is relatively low before annealing ($\eta_{emitter}$ = 38.7%) and increases to 50.8% after annealing (Table S1, Supporting Information). SEM images (**Figure 4**a–d) show that the edges of the nanocavities remain sharp after annealing. The nanocavity diameter distributions broaden slightly (Figure 4e,f), but the mean diameters remain unchanged within our measurement error (Table S1, Supporting Information). As shown in Figure 4g, after 12 h annealing at 1273 K, the W (1 1 0) peak is slightly shifted, and the full-width half-maximum (FWHM) of the peak is significantly narrowed. This is mainly attributed to the release of microstrain accumulated during atomic layer deposition process and a phase transition from the as-deposited nanocrystalline W to alpha-phase (bcc) W. After 168 h annealing at 1273 K (Figure S4, Supporting Information), the minor narrowing of the FWHM of the W (1 1 0) and W (2 0 0) peaks demonstrates a 19.6% reduction of microstrain and 3.5% growth of crystallite size, according to the Williamson–Hall plot.[64] The increased crystallinity and the denser coating layer result in higher optical reflectivity (metallicity) in the near infrared range,[27,65,66] thereby suppressing the thermal emission above the spectral cutoffs and improving the overall performance.

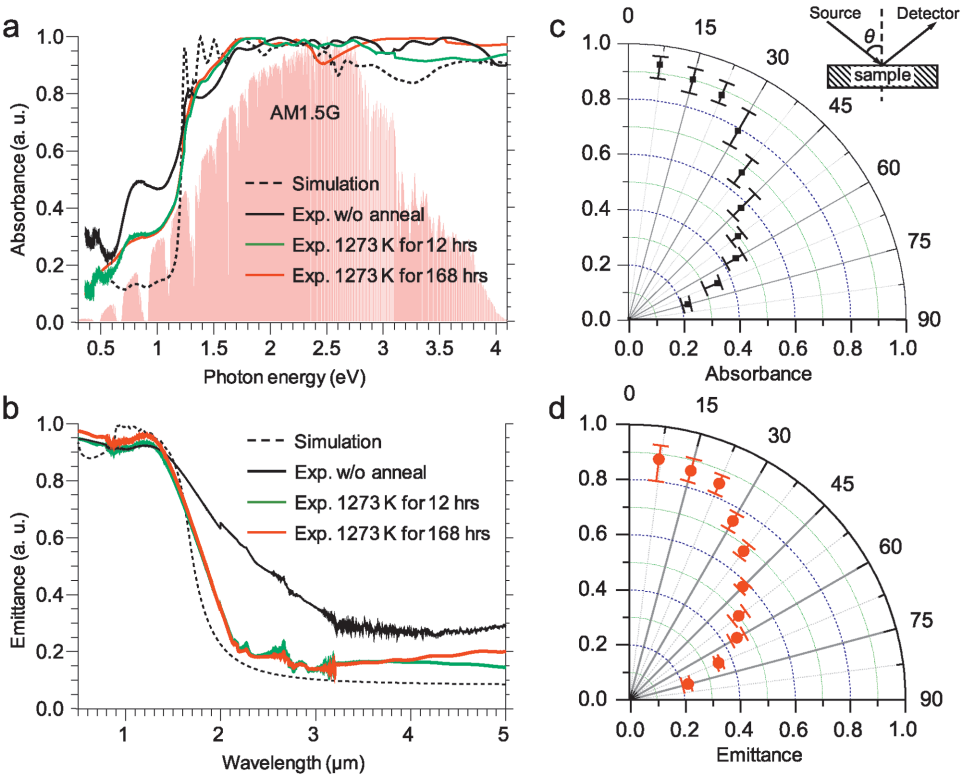

Figure 3. Optical properties of the fabricated W-CNT PhCs. a,b) Spectral absorbance and emittance of the W-CNT nanophotonic absorber and emitter before annealing, and after 12 and 168 h annealing at 1273 K, compared with the corresponding simulation values. c,d) Dependence of the average absorbance and emittance (300–800 nm) on the incidence angles for the W-CNT absorber and emitter. The angle θ is defined at the upper right.

The rate of the surface diffusion of metals at elevated temperatures is proportional to the divergence of the gradient of the local mean curvature of the surface.[28,67] For metal-based PhCs in prior work, the edges of the nanocavities have the largest local mean curvature and hence the highest surface diffusion velocity. This has resulted in the rounding and collapse of the nanocavity edges, and thus the deterioration of spectral selectivity at high temperatures.[28,50] In our work, the nanocavities in the W-CNT PhCs are realized by infiltration of the nanopatterned CNT forests with W, rather than top-down etching of a single material. Our approach avoids residual etching contaminants and process-induced surface defects which are known to degrade surface integrity of W.[68–70] The geometry of our pattern is intrinsically stable, as the surface diffusion rate over the whole W-CNT PhCs is uniform, and the diffusion of W in between individual Al_2O_3-coated CNTs is not energetically favorable.

In Figure 4h, the thermal stability of the present W-CNT PhCs is compared with data from previous studies of PhCs made of various materials.[20,22–27,29,32,56] We categorize this comparison according to the degradation of the absorber and emitter efficiency. Among reported thermal stability tests carried out for longer than 48 h,[26,56] our W-CNT PhCs (without a protective coating) sustain the highest annealing temperature (1273 K) without degradation. With HfO_2 as the protection layer, planar Ta-W PhCs showed minor degradation after 24 h annealing at 1473 K,[29] while 3D inverse opal W PhCs showed severe degradation after 1 h annealing at 1673 K.[24] Although a HfO_2 protection layer has been widely shown to improve thermal stability of PhCs,[24,25,29,56] concern arises due to the scarcity and high processing cost of Hf.[33,34] It was clarified by Peykov et al.[28] that the dominant failure mechanism for refractory metal-based PhCs at high temperature is surface diffusion. The surface diffusion rate of W increases by ≈10 times with every 200 K increase in temperature. For the W-CNT structure, the effect of local mean curvature could be mitigated because of support from the CNT scaffold. This makes the thermal stability of W-CNT PhCs comparably superior to those tested at higher temperatures.

In laboratory-scale STPV modules developed so far,[12,13,19,71] the input power and operating temperature have been limited below 1000 kW m^{-2} and 1300 K, respectively. Our results show promise to enable higher temperature STPV modules. To conclude this study, we estimate the power conversion efficiency of a planar STPV system with the W-CNT nanophotonic absorber and emitter placed over a GaSb PV cell. A 1D thermal diode model utilizes the experimentally measured spectral properties of the W-CNT PhCs to predict the STPV system efficiency at input powers (100–3000 kW m^{-2}) and operating temperatures (1000–2500 K). The model neglects the thermal loss from the system support and packaging as well as the resistive loss from the PV cell. This assumption is reasonable, because the major loss mechanisms for a large-scale planar STPV system are the re-emission from absorber to environment and above-bandgap emission from emitter to PV cell.[12,13,19] As shown in **Figure 5**a, at modest input powers (<1000 kW m^{-2}), $\eta_{absorber}$ exceeds 90%

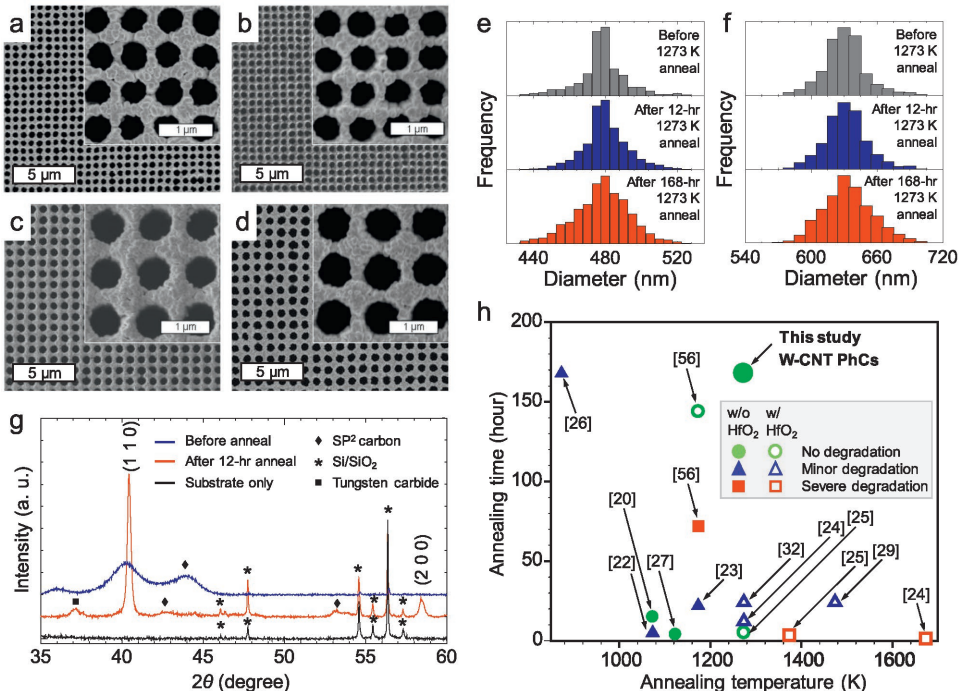

Figure 4. Thermal stability of the W-CNT PhCs. SEM images of a,b) the W-CNT nanophotonic absorber and c,d) the W-CNT nanophotonic emitter, after 12 and 168 h annealing at 1273 K. e,f) Histograms of the nanocavity size distribution of the W-CNT nanophotonic absorber and emitter before and after annealing at 1273 K, respectively. g) XRD spectra of the W-CNT nanophotonic surface before and after 12 h annealing at 1273 K, using the Si/SiO_2 substrate as reference. h) Comparison of thermal stability of the W-CNT PhCs to previously reported PhCs: ref. [20] TiN, ref. [22] $Ni-Al_2O_3$, ref. [23] $Au-Al_2O_3$, refs. [24,25] $W-HfO_2$, ref. [26] W-Ni-YSZ, ref. [27] $W-Al_2O_3$, ref. [29] Ta-$W-HfO_2$, Ref. [32] $Ru-HfO_2$, and ref. [56] $Ta-HfO_2$. No degradation, minor degradation, and severe degradation denote 0–5%, 5–15%, and greater than 15% degradation of absorber/emitter efficiency, respectively.

at relatively low operating temperatures (1000–1400 K). Figure 5b shows the operating temperature at which $\eta_{emitter}$ is maximized shifts upward with PV cell bandgap. At the thermally stable temperature (1273 K), the maximum $\eta_{emitter}$ of the W-CNT emitter is 54%, corresponding to the PV bandgap of 0.5 eV. The modeling results indicate that the integrated W-CNT nanophotonic absorber and emitter pair are promising as a thermal rectifier between the Sun and the PV cell at the thermally stable temperature (1273 K).

The STPV system efficiency (η_{system}) is a product of $\eta_{absorber}$, $\eta_{emitter}$ as well as the correction factors of the PV cell.[72] Figure 5c shows at the thermally stable operating temperature (1273 K), the predicted efficiency of the STPV system exceeds the SQ efficiency limit of the PV cell (23%) under a modest input power of 100 kW m^{-2}, and reaches as high as 33% under an input power of 1000 kW m^{-2}. Simultaneously increasing the input power to 3000 kW m^{-2} and operating temperature to 2000 K results in an increase of η_{system} to 41%. However, higher input power and operating temperature would increase the cost and thermal loss, respectively, which would counteract the moderate improvement. Therefore, while scientifically interesting, we feel the pursuit of even higher-temperature thermal stability of the W-CNT PhCs not necessary for practical implementation of our technology.

The predicted maximum efficiency of the STPV system with the W-CNT nanophotonic absorber and emitter are compared with prior estimates using different absorbers and emitters,[12,13,18,72,73] as shown in Figure 5d. Our predicted performance is especially superior at lower input powers (<500 kW m^{-2}), exceeding the predicted performance using Ta-HfO_2 PhCs as the absorber and emitter,[18] VACNTs as the absorber and multilayer Si/SiO_2 as the emitter,[12,13] as well as liquid Si as the absorber and liquid Sn as the emitter.[73] At higher input powers (>1000 kW m^{-2}), we predict slightly higher maximum system efficiency than a published model using tungsten pyramid nanostructures as the absorber and emitter.[72] By utilizing additional rugate filters,[13,74] the STPV system efficiency could be further improved.

In summary, we have explored a new W-CNT composite material for 2D PhCs. The fabricated W-CNT PhCs exhibit excellent spectral and angular selectivity as well as outstanding thermal stability after high-temperature annealing. Importantly, our process is intrinsically scalable; holographic interferometry can be performed with simple optical setup in the ambient; both CNT growth and ALD are vapor-phase processes which can be deployed in a roll-to-roll fashion; and no conventional masks or scanning lithography methods are required. Therefore, beyond STPV systems, CNT-based composite nanophotonic surfaces are also promising to be applied in other high-temperature energy conversion devices, such as photothermionic energy converters,[75] solar thermoelectric converters,[76] and thermophotonic solar cells.[77] In addition, the general strategy of nanopatterned CNT growth followed by vapor-phase infiltration of a solid matrix may be applied to engineer electromagnetic metasurfaces for a variety of needs.

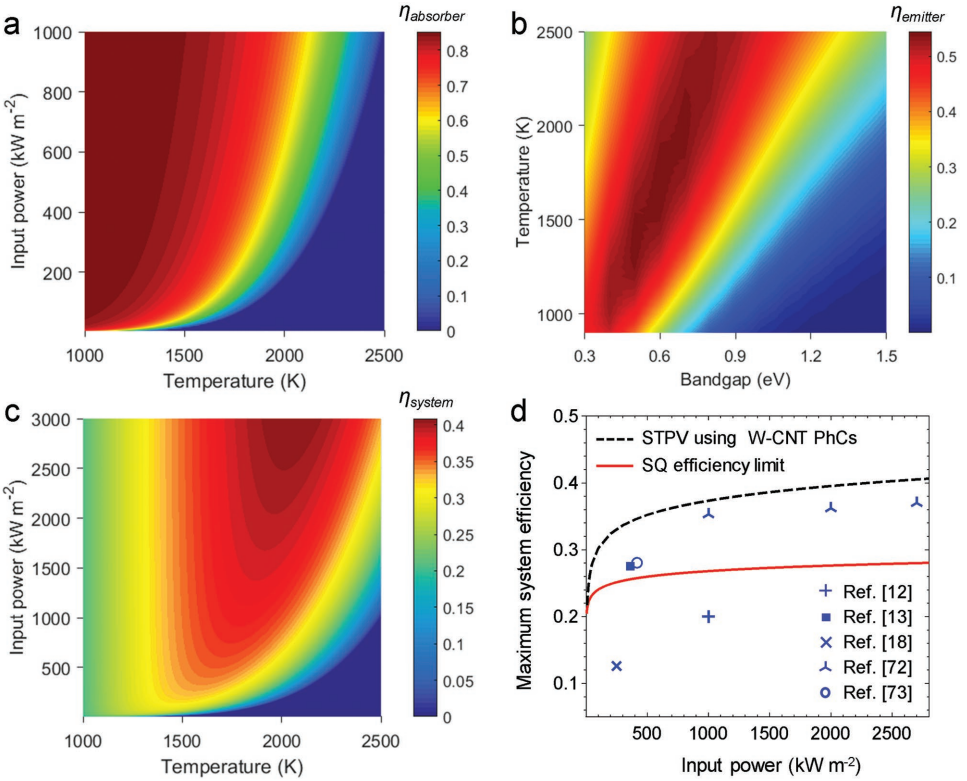

Figure 5. Simulated performance of a STPV system incorporating the measured spectral properties of the W-CNT absorber and emitter. a) Absorber efficiency of the STPV system versus solar input power and operating temperature. b) Emitter efficiency of the STPV system versus PV bandgap and operating temperature. c) Predicted STPV system efficiency versus solar input power and operating temperature. d) Predicted maximum STPV system efficiency, compared to the SQ efficiency limit, and to the predicted maximum system efficiencies using: refs. [12,13] VACNT as the absorber and multilayer Si/SiO_2 as the emitter, ref. [18] Ta-HfO_2 PhCs as the absorber and emitter, ref. [72] tungsten pyramid nanostructures as the absorber and emitter, and ref. [73] liquid Si as the absorber and liquid Sn as the emitter.

Experimental Section

CNT Catalyst Deposition: The catalyst composed of Fe (1 nm) upon Al_2O_3 (10 nm) was deposited by electron beam evaporation (VES-2550, Temescal) on a Si wafer (0.5 mm) with a thermally grown oxide layer (200 nm).

Catalyst Nanopatterning Using Nanoscale Holographic Interferometry: A bilayer stack of a bottom anti-reflection coating (BARC, Brewer Science XHRi-16) and a negative photoresist layer (Futurrex NR7-250) was spin-coated on the catalyst-coated Si substrate, followed by baking at 180 °C for 1 min. The bilayer stack was exposed to the HeCd laser using a Lloyd's mirror setup (Figure S3, Supporting Information). The periodicity of the nanopattern is given by $(\lambda/2)/\sin(\theta/2)$, where $\lambda = 325$ nm is the HeCd laser wavelength, and θ is the angle of the Lloyd's mirror. The achievable periodicity range is from ≈175 to ≈1500 nm. The pattern was then developed by immersion of the substrate in the mixture of tetramethylammonium hydroxide (Futurrex RD-6) and water with volume ratio of 3:1 for 40 s. The exposed BARC and catalyst layers were sequentially removed by He-O_2 (20%) RF plasma dry etching (Plasma-Therm, 200 W, 7 mTorr) for 2 min and immersion in 1 M NaOH for 1 min. A scotch tape was then applied and exfoliated manually to remove the residues and contaminants.

Synthesis of High-Density VACNTs: The HD-VACNTs were synthesized using a carbon preconditioning dynamic CVD process. The CVD system was fully automated with an in situ monitoring camera, i.e., Robofurnace.[78,79] A thin layer of carbon was first deposited on the inner wall of the CVD chamber at 750 °C by the flow mixture of 100 sccm C_2H_4 (99.9%, Airgas), 200 sccm H_2 (99.999%, Airgas), and 400 sccm wet He (100 ppm H_2O) for 5 min. With the system temperature maintained at 750 °C, a transfer arm carrying a Si/SiO_2 substrate loaded with the catalysts was inserted into the hot chamber with 400 sccm H_2 and 100 sccm dry He (99.999%, Airgas). After annealing at 750 °C for 10 min, the substrate was retracted from the hot chamber to cool down. The precursors—100 sccm C_2H_4, 200 sccm H_2, 200 sccm wet He, and 800 sccm dry He—were then introduced into the hot chamber. The substrate was inserted again after the stabilization of the precursor flow (≈5 min) for the synthesis of the HD-VACNTs. The typical growth rate of the CNT array was 2 μm s^{-1}. After reaching the desired CNT thickness, the growth was terminated by withdrawing the substrate from the reactor using the transfer arm under dry He purge.

Atomic Layer Deposition: Before the metallic tungsten ALD process, a 2 nm thick and conformal Al_2O_3 layer was deposited on the CNT arrays by 30 cycles of ALD (Gemstar XT, Arradiance Corporation) using ozone (generated by Pacific Ozone, using O_2 99.999% purity from Airgas) and TMA (98% purity, STREM Chemicals) as precursors. The Al_2O_3 deposition rate was ≈0.06 nm per cycle. The W ALD process was performed in a home-built flow tube reactor at 220 °C, with an inert Ar carrier flow rate of 210 sccm, to produce a baseline pressure of 1.5 Torr.[80] The W ALD process (35 cycles) was realized by alternately exposing the Al_2O_3-coated CNT arrays to diluted WF_6 (99.9%, Sigma-Aldrich) and SiH_4. The SiH_4 was a dilute mixture (2% by weight) in 99.999% Ar (Custom Gas Solutions). The carrier and purge gas was 99.999% pure N_2, and it passed through an inert gas purifier (Entegris GateKeeper) to remove residual water before entering the reactor. Typical precursor exposures in Langmuir (1 L = 10^{-6} Torr s) were ≈6×10^5 Langmuir, 5×10^5 Langmuir, and 1×10^7 Langmuir for SiH_4, WF_6, and Ar, respectively. The W deposition rate was ≈0.5–1 nm per cycle. Then, the as-deposited W-CNT composites were annealed at 1073 K for 1 h to help densify and stabilize W.

Annealing: The W-CNT samples were annealed in a tube furnace (Carbolite 3-zone furnace). Before annealing, the quartz tube was fully evacuated and re-charged with He (99.999%, Airgas), and repeated for three time to remove residue oxygen and water (below 0.1 ppm). The furnace was heated at a rate of 200 degree Celcius/hour until the target temperature with 150 sccm He flow, under a pressure below 10^{-3} Torr. After annealing, the samples were cooled down in the tube furnace under the same pressure and gas flow until room temperature.

FDTD Numerical Simulation: The nanophotonic surface was designed based on FDTD method, using MEEP package. The material dispersion of the W-CNT composite material was obtained by curve fitting of the measured reflectance (Figure 1b) using the Lorentz–Drude model. The parameters of the 3D FDTD simulation include a Gaussian distributed source (with electric field polarized in the *x* direction), periodic boundary conditions in the *x* and *y* directions, as well as perfectly matched layers on top and bottom of the unit cell. The design of the W-CNT nanophotonic surface was optimized by performing a series of simulations in which the values of periodicity *a*, nanocavity diameter *d* and thickness *t* were independently varied. The absorbance and emittance values were calculated by Kirchhoff's law based on the simulated reflectance and transmittance.

Characterization: SEM imaging was performed by Zeiss Merlin with Gemini II column. The surface roughness was characterized by AFM (Veeco Metrology Nanoscope IV). The optical properties were measured by UV–vis–NIR transmission/reflectance spectrophotometer (Varian/Cary-5000) using a commercial reference aluminum coated mirror (Thorlabs). The angular dependence of the optical properties was measured using a variable angle spectral reflectance accessory (VASRA). Thin-film X-ray diffraction was performed using Rigaku Smartlab.

Supporting Information

Supporting Information is available from the Wiley Online Library or from the author.

Acknowledgements

This work was supported by the MIT-Skoltech Initiative, by Lockheed Martin Corporation, and by faculty startup funds to A.J.H. from the Department of Mechanical Engineering at MIT. G.P acknowledges support from Semiconductor Research Corporation (SRC task #2401.001) and the National Science Foundation (CBET-1704151). Interference lithography was carried out at the NanoStructures Laboratory at MIT. CNT catalyst deposition was conducted at the Microsystems Technology Laboratories at MIT. Spectroscopy and electron microscopy were performed at the MIT Center for Materials Science and Engineering (CMSE), supported by the National Science Foundation (DMR-0819762).

Conflict of Interest

The authors declare no conflict of interest.

Keywords

carbon nanotubes, nanomanufacturing, photonic crystal, thermal stability, thermophotovoltaics

Received: May 14, 2018
Published online: August 13, 2018

[1] J. Zhou, X. Chen, L. J. Guo, *Adv. Mater.* **2016**, *28*, 3017.
[2] O. Ilic, P. Bermel, G. Chen, J. D. Joannopoulos, I. Celanovic, M. Soljačić, *Nat. Nanotechnol.* **2016**, *11*, 320.
[3] J.-J. Greffet, R. Carminati, K. Joulain, J.-P. Mulet, S. Mainguy, Y. Chen, *Nature* **2002**, *416*, 61.
[4] Z. Xie, K. Cao, Y. Zhao, L. Bai, H. Gu, H. Xu, Z.-Z. Gu, *Adv. Mater.* **2014**, *26*, 2413.
[5] C. Fenzl, T. Hirsch, O. S. Wolfbeis, *Angew. Chem., Int. Ed.* **2014**, *53*, 3318.
[6] A. M. Cubillas, S. Unterkofler, T. G. Euser, B. J. M. Etzold, A. C. Jones, P. J. Sadler, P. Wasserscheid, P. S. J. Russell, *Chem. Soc. Rev.* **2013**, *42*, 8629.
[7] T. Inoue, M. D. Zoysa, T. Asano, S. Noda, *Nat. Mater.* **2014**, *13*, 928.
[8] A. P. Raman, M. A. Anoma, L. Zhu, E. Rephaeli, S. Fan, *Nature* **2014**, *515*, 540.
[9] Z. Chen, L. Zhu, A. Raman, S. Fan, *Nat. Commun.* **2016**, *7*, 13729.
[10] Y. Zhai, Y. Ma, S. N. David, D. Zhao, R. Lou, G. Tan, R. Yang, X. Yin, *Science* **2017**, *355*, 1062.
[11] G. T. England, C. Russell, E. Shirman, T. Kay, N. Vogel, J. Aizenberg, *Adv. Mater.* **2017**, *29*, 1606876.
[12] A. Lenert, D. M. Bierman, Y. Nam, W. R. Chan, I. Celanovic, M. Soljacic, E. N. Wang, *Nat. Nanotechnol.* **2014**, *9*, 126.
[13] D. M. Bierman, A. Lenert, W. R. Chan, B. Bhatia, I. Celanović, M. Soljačić, E. N. Wang, *Nat. Energy* **2016**, *1*, 16068.
[14] W. R. Chan, P. Bermel, R. C. N. Pilawa-Podgurski, C. H. Marton, K. F. Jensen, J. J. Senkevich, J. D. Joannopoulos, M. Soljačić, I. Celanovic, *Proc. Natl. Acad. Sci. USA* **2013**, *110*, 5309.
[15] Y. X. Yeng, M. Ghebrebrhan, P. Bermel, W. R. Chan, J. D. Joannopoulos, M. Soljačić, I. Celanovic, *Proc. Nat. Acad. Sci. USA* **2012**, *109*, 2280.
[16] H. Kolm, *MIT Lincoln Laboratory Quarterly Progress Report*, **1956**, *35*, 13.
[17] W. Shockley, H. J. Queisser, *J. Appl. Phys.* **1961**, *32*, 510.
[18] W. R. Chan, V. Stelmakh, M. Ghebrebrhan, M. Soljacic, J. D. Joannopoulos, I. Celanovic, *Energy Environ. Sci.* **2017**, *10*, 1367.
[19] V. Rinnerbauer, A. Lenert, D. M. Bierman, Y. X. Yeng, W. R. Chan, R. D. Geil, J. J. Senkevich, J. D. Joannopoulos, E. N. Wang, M. Soljačić, I. Celanovic, *Adv. Energy Mater.* **2014**, *4*, 1400334.
[20] W. Li, U. Guler, N. Kinsey, G. V. Naik, A. Boltasseva, J. Guan, V. M. Shalaev, A. V. Kildishev, *Adv. Mater.* **2014**, *26*, 7959.
[21] V. Rinnerbauer, E. Lausecker, F. Schäffler, P. Reininger, G. Strasser, R. D. Geil, J. D. Joannopoulos, M. Soljačić, I. Celanovic, *Optica* **2015**, *2*, 743.
[22] P. Li, B. Liu, Y. Ni, K. K. Liew, J. Sze, S. Chen, S. Shen, *Adv. Mater.* **2015**, *27*, 4585.
[23] Z. J. Coppens, I. I. Kravchenko, J. G. Valentine, *Adv. Opt. Mater.* **2016**, *4*, 671.
[24] K. A. Arpin, M. D. Losego, A. N. Cloud, H. Ning, J. Mallek, N. P. Sergeant, L. Zhu, Z. Yu, B. Kalanyan, G. N. Parsons, G. S. Girolami, J. R. Abelson, S. Fan, P. V. Braun, *Nat. Commun.* **2013**, *4*, 2630.
[25] P. N. Dyachenko, S. Molesky, A. Y. Petrov, M. Stormer, T. Krekeler, S. Lang, M. Ritter, Z. Jacob, M. Eich, *Nat. Commun.* **2016**, *7*, 11809.
[26] F. Cao, D. Kraemer, L. Tang, Y. Li, A. P. Litvinchuk, J. Bao, G. Chen, Z. Ren, *Energy Environ. Sci.* **2015**, *8*, 3040.
[27] M. Chirumamilla, A. S. Roberts, F. Ding, D. Wang, P. K. Kristensen, S. I. Bozhevolnyi, K. Pedersen, *Opt. Mater. Express* **2016**, *6*, 2704.
[28] D. Peykov, Y. X. Yeng, I. Celanovic, J. D. Joannopoulos, C. A. Schuh, *Opt. Express* **2015**, *23*, 9979.
[29] V. Stelmakh, V. Rinnerbauer, R. D. Geil, P. R. Aimone, J. J. Senkevich, J. D. Joannopoulos, M. Soljačić, I. Celanovic, *Appl. Phys. Lett.* **2013**, *103*, 123903.
[30] V. Rinnerbauer, S. Ndao, Y. X. Yeng, W. R. Chan, J. J. Senkevich, J. D. Joannopoulos, M. Soljacic, I. Celanovic, *Energy Environ. Sci.* **2012**, *5*, 8815.

[31] V. Stelmakh, W. R. Chan, M. Ghebrebrhan, J. Senkevich, J. D. Joannopoulos, M. Soljačić, I. Celanović, *IEEE Trans. Nanotechnol.* **2016**, *15*, 303.
[32] J. B. Chou, Y. X. Yeng, Y. E. Lee, A. Lenert, V. Rinnerbauer, I. Celanovic, M. Soljacic, N. X. Fang, E. N. Wang, S.-G. Kim, *Adv. Mater.* **2014**, *26*, 8041.
[33] J. R. Dodson, A. J. Hunt, H. L. Parker, Y. Yang, J. H. Clark, *Chem. Eng. Process.* **2012**, *51*, 69.
[34] M. L. C. M. Henckens, P. P. J. Driessen, E. Worrell, *Resour., Conserv. Recycl.* **2014**, *93*, 1.
[35] Z.-P. Yang, L. Ci, J. A. Bur, S.-Y. Lin, P. M. Ajayan, *Nano Lett.* **2008**, *8*, 446.
[36] K. Mizuno, J. Ishii, H. Kishida, Y. Hayamizu, S. Yasuda, D. N. Futaba, M. Yumura, K. Hata, *Proc. Natl. Acad. Sci. USA* **2009**, *106*, 6044.
[37] A. B. Kuzmenko, E. van Heumen, F. Carbone, D. van der Marel, *Phys. Rev. Lett.* **2008**, *100*, 117401.
[38] O. J. A. Schueller, S. T. Brittain, G. M. Whitesides, *Adv. Mater.* **1997**, *9*, 477.
[39] G. M. Jenkins, K. Kawamura, *Nature* **1971**, *231*, 175.
[40] W. A. deHeer, W. S. Bacsa, A. Châtelain, T. Gerfin, R. Humphrey-Baker, L. Forro, D. Ugarte, *Science* **1995**, *268*, 845.
[41] F. J. García-Vidal, J. M. Pitarke, J. B. Pendry, *Phys. Rev. Lett.* **1997**, *78*, 4289.
[42] F. Cao, D. Kraemer, T. Sun, Y. Lan, G. Chen, Z. Ren, *Adv. Energy Mater.* **2015**, *5*, 1401042.
[43] I. Celanovic, N. Jovanovic, J. Kassakian, *Appl. Phys. Lett.* **2008**, *92*, 193101.
[44] A. F. Oskooi, D. Roundy, M. Ibanescu, P. Bermel, J. D. Joannopoulos, S. G. Johnson, *Comput. Phys. Commun.* **2010**, *181*, 687.
[45] M. Ghebrebrhan, P. Bermel, Y. X. Yeng, I. Celanovic, M. Soljačić, J. D. Joannopoulos, *Phys. Rev. A* **2011**, *83*, 033810.
[46] S. D. Elliott, G. Dey, Y. Maimaiti, H. Ablat, E. A. Filatova, G. N. Fomengia, *Adv. Mater.* **2016**, *28*, 5367.
[47] S. D. Elliott, G. Scarel, C. Wiemer, M. Fanciulli, G. Pavia, *Chem. Mater.* **2006**, *18*, 3764.
[48] S. Ahmad, D. Copic, C. George, M. De Volder, *Adv. Mater.* **2016**, *28*, 6705.
[49] S. Tawfick, M. De Volder, D. Copic, S. J. Park, C. R. Oliver, E. S. Polsen, M. J. Roberts, A. J. Hart, *Adv. Mater.* **2012**, *24*, 1628.
[50] S. A. Robert W. Balluffi, W. Craig Carter, *Kinetics of Materials*, Wiley Interscience, Hoboken, NJ **2005**.
[51] S. J. Pearton, F. Ren, C. R. Abernathy, *Semicond. Sci. Technol.* **1993**, *8*, 1897.
[52] W. Chu, K. W. Foster, L. M. Shirey, K. W. Rhee, J. Kosakowski, I. P. Isaacson, D. McCarthy, C. R. Eddy Jr., E. A. Dobisz, C. R. K. Marrian, M. C. Peckerar, *Appl. Phys. Lett.* **1994**, *64*, 2172.
[53] I. Wathuthanthri, Y. Liu, K. Du, W. Xu, C.-H. Choi, *Adv. Funct. Mater.* **2013**, *23*, 608.
[54] V. J. Cadarso, N. Chidambaram, L. Jacot-Descombes, H. Schift, *Microsyst. Nanoeng.* **2017**, *3*, 17017.
[55] P. Kim, W. E. Adorno-Martinez, M. Khan, J. Aizenberg, *Nat. Protoc.* **2012**, *7*, 311.
[56] V. Rinnerbauer, Y. X. Yeng, W. R. Chan, J. J. Senkevich, J. D. Joannopoulos, M. Soljačić, I. Celanovic, *Opt. Express* **2013**, *21*, 11482.
[57] N. Selvakumar, S. B. Krupanidhi, H. C. Barshilia, *Adv. Mater.* **2014**, *26*, 2552.
[58] T. Saleh, M. V. Moghaddam, M. S. M. Ali, M. Dahmardeh, C. A. Foell, A. Nojeh, K. Takahata, *Appl. Phys. Lett.* **2012**, *101*, 061913.
[59] B. D. Wood, J. S. Dyer, V. A. Thurgood, N. A. Tomlin, J. H. Lehman, T.-C. Shen, *J. Appl. Phys.* **2015**, *118*, 013106.
[60] E. D. Kosten, J. H. Atwater, J. Parsons, A. Polman, H. A. Atwater, *Light: Sci. Appl.* **2013**, *2*, e45.
[61] M. A. Green, S. P. Bremner, *Nat. Mater.* **2017**, *16*, 23.
[62] J. L. Balenzategui, F. Chenlo, *Sol. Energy Mater. Sol. Cell* **2005**, *86*, 53.
[63] V. Rinnerbauer, S. Ndao, Y. X. Yeng, J. J. Senkevich, K. F. Jensen, J. D. Joannopoulos, M. Soljačić, I. Celanovic, R. D. Geil, *J. Vac. Sci. Technol., B.* **2013**, *31*, 011802.
[64] H. P. Klug, L. E. Alexander, *X-Ray Diffraction Procedures: For Polycrystalline and Amorphous Materials*, 2nd ed., Wiley-Interscience, New York **1974**
[65] K. A. Arpin, M. D. Losego, P. V. Braun, *Chem. Mater.* **2011**, *23*, 4783.
[66] V. Stelmakh, V. Rinnerbauer, J. D. Joannopoulos, M. Soljačić, I. Celanovic, J. J. Senkevich, C. Tucker, T. Ives, R. Shrader, *J. Vac. Sci. Technol., A* **2013**, *31*, 061505.
[67] J. W. Cahn, J. E. Taylor, *Acta Mater.* **1994**, *42*, 1045.
[68] J. J. Bellina Jr., H. E. Farnsworth, *J. Vac. Sci. Technol.* **1972**, *9*, 616.
[69] H. Fan, Y. You, W. Ni, Q. Yang, L. Liu, G. Benstetter, D. Liu, C. Liu, *Sci. Rep.* **2016**, *6*, 23738.
[70] G. Turban, J. F. Coulon, N. Mutsukura, *Thin Solid Films* **1989**, *176*, 289.
[71] A. Datas, C. Algora, *Prog. Photovoltaics: Res. Appl.* **2013**, *21*, 1025.
[72] E. Rephaeli, S. Fan, *Opt. Express* **2009**, *17*, 15145.
[73] H. R. Seyf, A. Henry, *Energy Environ. Sci.* **2016**, *9*, 2654.
[74] D. Chester, P. Bermel, J. D. Joannopoulos, M. Soljacic, I. Celanovic, *Opt. Express* **2011**, *19*, A245.
[75] J. W. Schwede, I. Bargatin, D. C. Riley, B. E. Hardin, S. J. Rosenthal, Y. Sun, F. Schmitt, P. Pianetta, R. T. Howe, Z.-X. Shen, N. A. Melosh, *Nat. Mater.* **2010**, *9*, 762.
[76] D. Kraemer, Q. Jie, K. McEnaney, F. Cao, W. Liu, L. A. Weinstein, J. Loomis, Z. Ren, G. Chen, *Nat. Energy* **2016**, *1*, 16153.
[77] D. J. Farrell, H. Sodabanlu, Y. Wang, M. Sugiyama, Y. Okada, *Nat. Commun.* **2015**, *6*, 8685.
[78] J. Li, M. Bedewy, A. O. White, E. S. Polsen, S. Tawfick, A. J. Hart, *J. Phys. Chem. C* **2016**, *120*, 11277.
[79] C. R. Oliver, W. Westrick, J. Koehler, A. Brieland-Shoultz, I. Anagnostopoulos-Politis, T. Cruz-Gonzalez, A. J. Hart, *Rev. Sci. Instrum.* **2013**, *84*, 115105.
[80] B. Kalanyan, M. D. Losego, C. J. Oldham, G. N. Parsons, *Chem. Vap. Deposition* **2013**, *19*, 161.

